Using the Angular Dependence of the Polarization Ratio to Analyze Aircraft Passive Microwave Measurements Over Land

Richard de Jeu, *Member, IEEE*, Susan S. Steele-Dunne, Timothy Lang, Corey G. Amiot, Marian Klein, *Member, IEEE*, Madison Eble, and Diego G. Miralles

***Abstract*—The derivation of geophysical parameters from passive microwave observations over land has always been challenging. Soil conditions, land cover, and the atmosphere affect the measurements to varying degrees, and it is difficult to isolate these individual contributions. In this study, we assess whether multiangle observations provide additional information that can strengthen existing retrieval algorithms. Between October and November 2024, a series of airborne flights carrying the advanced microwave precipitation radiometer (AMPR) were conducted over the United States. Three land-based flights with multiangle observations from 0° to 45° and dual-polarized measurements at 10.7, 19.35, and 37.1 GHz were analyzed. The data showed a strong linear relationship between the microwave polarization ratio and the incidence angles within the 25°–45° range (e.g., $R^2 > 0.9$ for 71.2% of all flight scans analyzed at 10.7 GHz). The linear model for the polarization ratio showed a similar performance in terms of root-mean-square error (RMSE) to simulations based on a τ–ω radiative transfer model and commonly used assumptions. The observed linearity was further evaluated with satellite observations from the AMSR2. This evaluation confirmed the observed linearity across all three frequencies. The slope of the relationship between the polarization ratio and the incidence angle was calculated for each multiangle flight scan, which was sensitive to both soil moisture (SM) and vegetation. This new parameter, which was derived from multiple observations, appeared to be consistent in time and space, revealing similar patterns along flight lines acquired at different times. The slope was used as input in regression models (RMs) to derive SM. A model solely based on 10.7-GHz data revealed a strong correlation ($R^2 = 0.81$) with Level-3 SM from the SM active passive (SMAP) mission, demonstrating the potential of multiangle retrievals with established SM products.**

***Index Terms*—Airborne remote sensing, multiangle observations, passive microwave radiometry, polarization ratio.**

Received 2 October 2025; revised 12 December 2025 and 7 January 2026; accepted 15 January 2026. Date of publication 28 January 2026; date of current version 6 February 2026. This work was supported by European Space Agency (ESA) Climate Change Initiative (CCI) Plus Soil Moisture Project (ESRIN) under Contract 400012668/19/1-NB. *(Corresponding author: Richard de Jeu.)*

Richard de Jeu is with Transmissivity B.V., 2403 NA Alphen aan den Rijn, The Netherlands (e-mail: ries@transmissivitybv.nl).

Susan S. Steele-Dunne is with the Department of Geoscience and Remote Sensing, Delft University of Technology, 2628 CN Delft, The Netherlands.

Timothy Lang is with the Earth Science Branch, NASA Marshall Space Flight Center, Huntsville, AL 35812 USA.

Corey G. Amiot is with the Earth System Science Center, The University of Alabama in Huntsville, Huntsville, AL 35805 USA.

Marian Klein and Madison Eble are with Boulder Environmental Sciences and Technology, Boulder, CO 80301 USA.

Diego G. Miralles is with the Hydro-Climate Extremes Laboratory (H-CEL), Ghent University, B-9000 Ghent, Belgium.

Digital Object Identifier 10.1109/TGRS.2026.3657427

I. Introduction

THE interpretation of passive microwave observations over land has been a topic of scientific inquiry for several decades. The basic capabilities of these observations for soil moisture (SM) sensing are well understood [1]. Soil emissivity at low microwave frequencies (<20 GHz) is strongly influenced by moisture content due to the large dielectric contrast between dry soil and water. Fluctuations in SM can, therefore, be measured by microwave radiometers. However, many other factors also influence these observations, including surface roughness, soil type, vegetation cover, and atmospheric conditions, making their modeling challenging [2]. Microwave observations at multiple incidence angles could provide a means to disentangle these contributions.

In the active microwave domain, the added value of observations at different angles has been demonstrated. Satellite instruments with multiangle capabilities, such as the advanced scatterometer (ASCAT) of European Space Agency (ESA), were specifically designed for this purpose. The TU Wien change detection algorithm, for example, illustrates how angular dependence can be exploited by leveraging multiangle ASCAT observations to retrieve SM and vegetation dynamics [3], [4], [5], [6]. Other researchers also utilized the multiangle capabilities of this instrument to retrieve wind products [7]. In the passive domain, most microwave radiometers measuring in low frequencies (<20 GHz) have a fixed incidence angle. The only exception is the SM ocean salinity (SMOS) mission of ESA [8]. The SMOS payload consists of an interferometric radiometer operating in the L-band frequency (i.e., 1.4 GHz) across a range of incidence angles from 0° to 65°. In more than 15 years of operation, its multiangle measurements have shown many benefits compared to single-angle observations. The multiangle design of SMOS revealed a better physical separability of soil and vegetation parameters [9], [10], options for noise and bias mitigation through angular fitting or smoothing [11], and additional constraints in retrievals and data assimilation [12]. By contrast, single-angle missions, such as the SM active passive (SMAP), require angle normalization or alternative strategies to achieve similar ends.

The L-band frequency is considered ideal for SM retrieval. It has a soil penetration depth of a couple of centimeters, lower sensitivity to vegetation than higher frequencies, and is only weakly attenuated by the atmosphere. This is also the reason

why dedicated SM missions like SMAP and SMOS made use of this frequency. However, large (and expensive) antennas are required to derive reliable measurements, and the spatial resolution that can be achieved with these instruments is still coarse, on the order of several tens of kilometers. At higher frequencies (e.g., X-band, between 8 and 12 GHz), antennas are considerably smaller and provide reliable brightness temperatures at a much finer spatial resolution. An upcoming mission that will exploit this is ESA's Copernicus Imaging Microwave Radiometer (CIMR), which will be measuring at multiple frequencies. The spatial resolution of the proposed L-band instrument will be 58 km, whereas for X-band the resolution will be 15 km [13]. The penetration depth at X-band will be shallower (approximately 1 cm) than at L-band. However, with multiangle observations, it might be possible to better mitigate atmospheric and vegetation effects, leading to more accurate SM retrievals at this frequency.

Currently, one of the biggest threats to passive microwave remote sensing is the presence of radio frequency interference (RFI). RFI consists of unwanted electromagnetic emissions that degrade receiver performance, and observations from microwave radiometers can be strongly affected by such signals. The origin of RFI can be traced to various sources, ranging from accidental out-of-band emissions to intentional jamming [14]. Although most passive microwave radiometers operate in protected frequency bands, RFI contamination has been observed across multiple frequency bands, from L- to K-band [15], [16], [17]. For the derivation of geophysical parameters, it is therefore important not to focus on a single frequency but to maintain a broad perspective on what information other frequencies can provide.

Multiangle passive microwave observations at frequencies higher than L-band have been limited to a few field and aircraft experiments [18], [19], [20], [21]. With the recent availability of multiangle passive microwave data over land from the Westcoast and Heartland Hyperspectral Microwave Sensor Intensive Experiment (WH^{2}yMSIE, [22]), conducted in October and November 2024 and covered multiple landscapes in the United States, there is now an opportunity to further explore this potential. During WH^{2}yMSIE, passive microwave observations at four frequencies (i.e., 10.7, 19.35, 37.1, and 85.5 GHz) were collected with the Advanced Microwave Precipitation Radiometer (AMPR) [23].

The aim of this study is to examine the added value of the AMPR multiangle observations over land. To do so, we focus on the microwave polarization difference index (MPDI) and on how its angular dependence can be used to explain the different contributors to the signal, particularly vegetation and SM. This index is used because it can be directly calculated from measured dual-polarized brightness temperatures. The MPDI is defined as follows:

$$\mathrm{MPDI} = \frac{T_{b,[V]} - T_{b,[H]}}{T_{b,[V]} + T_{b,[H]}} \tag{1}$$

where T_b is the measured brightness temperature at polarization P ([V] or [H]). The MPDI is regarded as a powerful tool for characterizing soil and vegetation properties from microwave observations because it minimizes the influence of temperature (e.g., [24], [25], [26]). The angular response of the MPDI to different vegetation and moisture conditions for the AMPR observations at three frequencies (i.e., 10.7, 19.35, and 37.1 GHz) is explored using both a radiative transfer model and a statistical approach. In addition, the AMPR observations are compared with SMOS data to provide insights into the impact of scale and frequency. This analysis of multiangle observations will help advance our understanding of passive microwave observations over land.

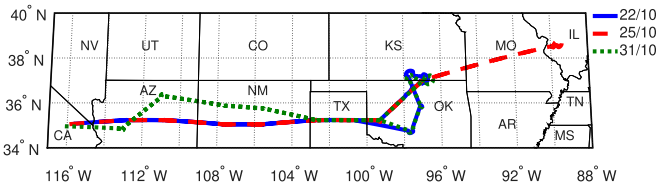

Fig. 1. ER-2 aircraft ground tracks as part of WH^{2}yMSIE over different states of U.S. for the three different flights over land.

II. Flight Campaign

The multiangle passive microwave data used in this study were collected during WH^{2}yMSIE [22]. This field campaign was a partnership between the National Aeronautics and Space Administration (NASA) and the National Oceanic and Atmospheric Administration (NOAA), with the aim of characterizing the thermodynamic structure of the planetary boundary layer (PBL). Hyperspectral microwave measurements, which provide thousands of channels in the 50–58- and 175–191-GHz ranges, were combined with data collected from other passive and active sensors by the NASA ER-2 aircraft. The ER-2 was chosen as the aircraft platform for WH^{2}yMSIE because it can fly over even the tallest thunderstorms. Ten flights were conducted between October 18, 2024 and November 13, 2024. Three of these flights flew over land and are used in the present study. The other seven flights were over the ocean. The tracks of the three flights over land are shown in Fig. 1. The flights departed from NASA Armstrong Flight Research Center in CA, flying first west to east and then returning east to west. On October 22, the aircraft crossed multiple states and turned around at the Atmospheric Radiation Measurement (ARM) Southern Great Plains (SGPs) Observatory in OK. On October 25, the aircraft flew farther and turned around in IL. On October 31, the flight was identical to that of October 22 over TX and OK, but the flight shifted slightly farther north over NM and AZ. The flights from east to west took place mainly between 17:00 and 20:00 h, and the return flights from west to east took place between approximately 20:00 and 23:00 h, all in UTC.

III. Data

A. Aircraft Data

Multiangle brightness temperatures were measured with AMPR at 10.7, 19.35, 37.1, and 85.5 GHz during the three ER-2 aircraft flights over land. AMPR consists of two lens-horn antenna systems and a reflector scanning system for data collection and calibration. The lens-horns were designed to

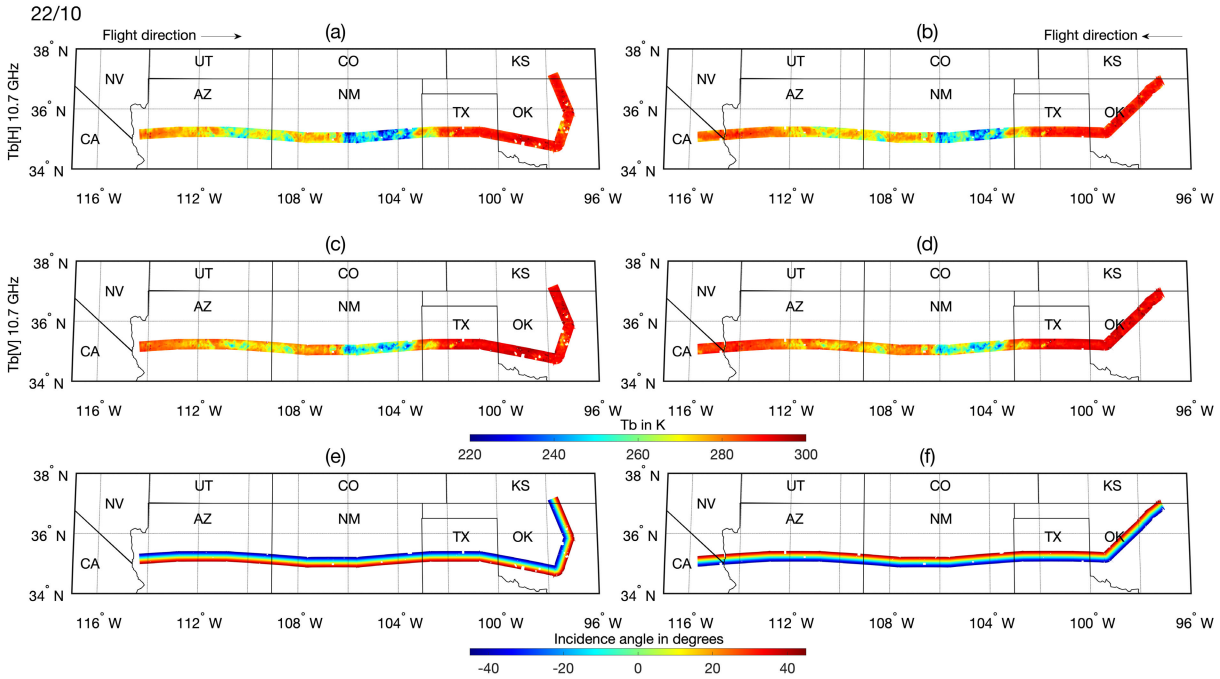

Fig. 2. AMPR brightness temperature (T_b) observations at 10.7 GHz for the land flight of October 22, 2024. (a) and (b) Horizontally polarized brightness temperatures. (c) and (d) Vertically polarized brightness temperatures. (e) and (f) Measured incidence angles.

have equal-size footprints at the two lowest frequencies (i.e., 19.35 and 10.7 GHz). This was done to facilitate accurate comparisons between these two frequencies. At the cruising aircraft altitude of 20 km, AMPR, measured with relative footprint sizes at the surface of 0.6 km (85.5 GHz), 1.5 km (37.1 GHz), and 2.8 km (19.35 and 10.7 GHz). Brightness temperatures were retrieved in both horizontal and vertical polarization with a radiometer temperature sensitivity between 0.2 and 0.5 K. The radiometer scanned the Earth surface between −45° and 45° angles in 50 steps across an approximately 40-km swath perpendicular to the flight line [23]. The data were sampled using the 85.5-GHz channel's 0.6 km footprint in cross-track direction, resulted in oversampling at the other three frequencies [27]. Data were prepared by NASA and for this study the AMPR WH^{2}yMSIE Science Dataset Level 2B, Version 1 (R1) [28] was used.

Prior to their use in this study, AMPR brightness temperatures were corrected for cross-track and absolute bias using radiative transfer adjustments following [27]. To aid with this, atmospheric profiles and ocean surface information from the global data assimilation system (GDAS) 6-h analysis product [29] were remapped onto the AMPR swath. Cloud-free, over-water portions of the October 23, 2024, November 7, 2024, and November 12, 2024 flights were combined and used to develop median brightness temperature slope corrections for all flights. The corrected mixed-polarization measurements at each frequency were then deconvolved to pure horizontal and vertical polarizations following [30].

The brightness temperatures from the three flights over land were selected, whereas the data at 85.5 GHz were excluded from this study because this frequency provides limited land surface information. Only observations with a land fraction larger than 90% and a stable high altitude (>19.8 km) were selected to exclude water-dominated pixels and minimize the variation in footprint size. Moreover, observations with incidence angle values beyond 45° caused by aircraft maneuvers as well as noisy data and outliers were excluded using the provided quality flags. Additional atmospheric radiative transfer modeling revealed a negligible atmospheric contribution to the signal for all three frequencies—more detailed information on this analysis can be found in Appendix A. Figs. 2 and 3 show the observed brightness temperatures at multiple angles for 10.7 GHz from the three different flights over land. The other frequencies (not shown) show similar patterns.

B. Satellite Data

AMSR2 level 1B brightness temperatures (version 2.2) were collected from the Global Portal System of Japan Aerospace Exploration Agency (JAXA). For this study, the dual-polarized data from 10.65, 18.7, and 36.5 GHz were selected for the dates and locations corresponding to aircraft overpasses on October 22, 25, and 31, 2024. The AMSR2 instrument is a conical-scanning passive microwave sensor, operating at an altitude of 700 km since July 2012. It has an ascending equator-crossing time of 1:30 P.M. and a descending time of 1:30 A.M. In this study, both the ascending and descending observations were used. The instrument has an incidence angle of 55°. The 10.65-GHz frequency has a bandwidth of 100 MHz and a ground resolution of 24 × 42 km^2. The 18.7-GHz frequency channel, which has a bandwidth of 200 MHz, provides a ground resolution of 14 × 22 km^2. The 36.5-GHz channel, with a bandwidth of 1000 MHz, provides a

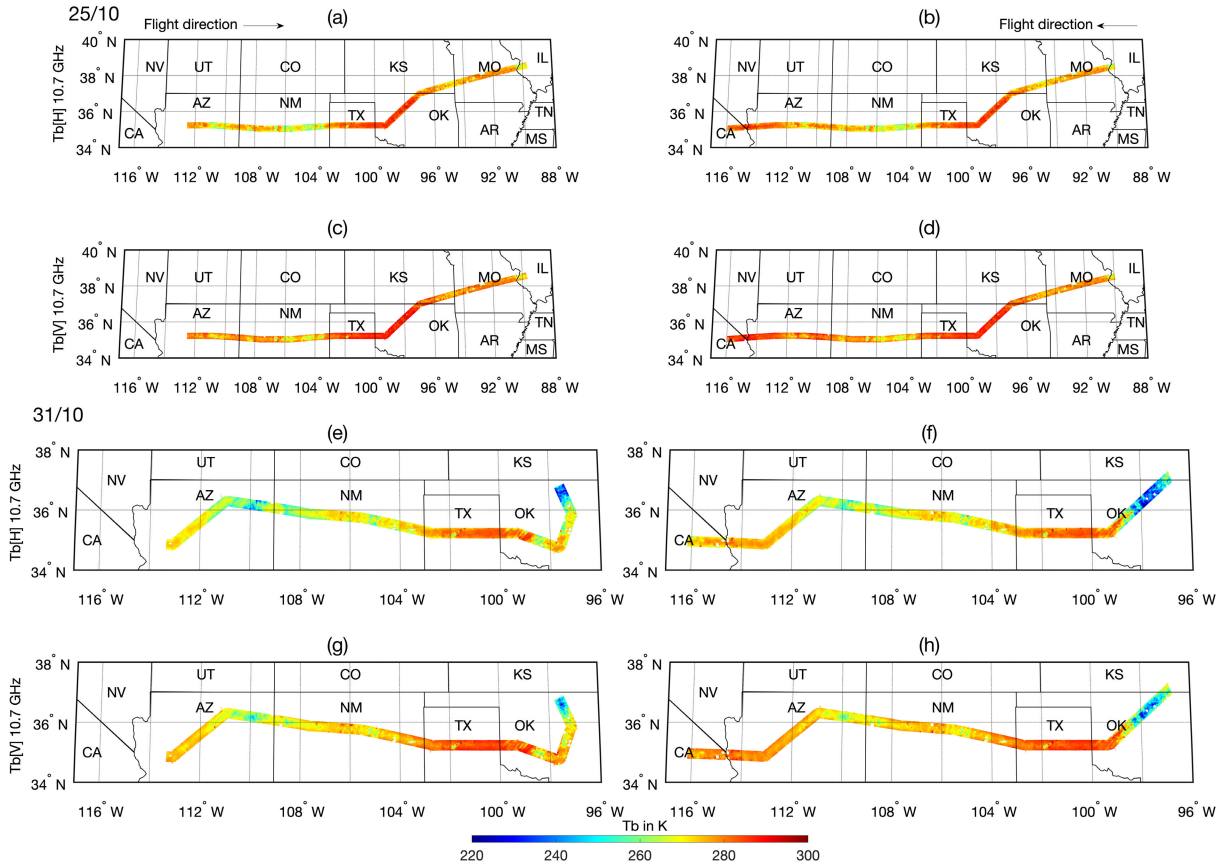

Fig. 3. AMPR brightness temperature (T_b) observations at 10.7 GHz for the land flight of October 25 and 31, 2024. (a), (b), (e), and (f) Horizontally polarized brightness temperatures. (c), (d), (g), and (h) Vertically polarized brightness temperatures.

ground resolution of 7×12 km^2. All channels had a sampling interval of 10 km [31].

The application for extraction and exploring analysis ready samples (AppEEARS) [32] was used as a tool to extract SM and vegetation information from SMAP and the moderate resolution imaging spectroradiometer (MODIS), respectively. SMAP Level 3 Radiometer global daily 9-km SM data (version 6), based on the dual channel algorithm (DCA, [33]), were obtained for the three days covering the different flight lines. Both datasets from the descending (with a local solar time of 6 A.M.) and ascending (with a local solar time of 6 P.M.) overpasses were used to achieve the highest coverage. SM information refers to the top few centimeters of the soil and is expressed in volumetric units ($m^3 \cdot m^{-3}$). Quality flags were used to screen the data for outliers and spurious values, and only SM values for which the retrievals were labeled as having recommended quality were used. In addition, due to the presence of low vegetation cover over the flight lines, the SM error was estimated to be within the 0.04-$m^3 \cdot m^{-3}$ range [34]. A 16-day MODIS normalized difference vegetation index (NDVI; MYD13A2 v6.1) image from October 23 was collected to represent the vegetation variability for the three different days.

Multiangle L-band (1.4 GHz) brightness temperature data from the ESA SMOS mission were obtained. In this study, the Center Aval de Traitement des Données SMOS (CATDS) Level-3 brightness temperatures dataset [35], [36] from operational processing was used. In this dataset, the horizontally and vertically polarized brightness temperatures are provided in the Equal-Area Scalable Earth 2 (EASE-2) grid [37] 25×25 km^2 grid-cell size. On each overpass, SMOS measures an incidence-angle profile of the brightness temperature ranging from 0° to 65°. The brightness temperatures used in this study were selected for the region between 34°N and 40°N, and 117°W and 88°W for the three flight days in October 2024. Data from the descending (6 A.M.) overpass and ascending (6 P.M.) overpass were used. The provided quality flags were used to screen for potential contamination caused by the Sun or RFI.

IV. Methods

A. Microwave Model

Brightness temperatures measured by microwave radiometers can be simulated using radiative transfer models. The most widely used model is the τ–ω model [38], which describes microwave emission from a land surface with a vegetation cover through three terms: 1) soil radiation attenuated by vegetation; 2) direct vegetation emission; and 3) vegetation downward radiation reflected by the soil and attenuated by the canopy. When the atmospheric contribution is also taken into account, the observed brightness temperatures (T_b) at

polarization P ([V] or [H]), as measured by a satellite or aircraft, can be expressed as follows:

$$T_{b,P} = T_{b,\mathrm{au},P} + \Gamma_a \left[\Gamma_v e_{\mathrm{rs},P} T_s + (1-\Gamma_v)(1-\omega) T_v + (1-\Gamma_v)(1-w) T_v \left(1-e_{\mathrm{rs},P}\right)\Gamma_v + T_{b,\mathrm{ad},P}\left(1-e_{\mathrm{rs},P}\right)\Gamma_v^2\right] \quad (2)$$

where $T_{b,\mathrm{au},P}$ and $T_{b,\mathrm{ad},P}$ are the upward and downward atmospheric brightness temperatures, respectively, and Γ_a is the atmospheric transmissivity. Γ_v is the vegetation transmissivity, ω is the single scattering albedo of the vegetation, and $e_{\mathrm{rs},P}$ is the rough surface emissivity. T_s is the soil temperature and T_v is the vegetation canopy temperature, both in Kelvin. The vegetation transmissivity is a function of the vegetation optical depth (τ_v) and the incidence angle (u), such that

$$\Gamma_v = \exp^{-\tau_v \sec(u)}. \quad (3)$$

The rough surface emissivity ($e_{\mathrm{rs},P}$), which is equal to 1 minus the rough surface reflectivity ($R_{\mathrm{rs},P}$), can be derived from Fresnel relationships in combination with a roughness model. The Fresnel relations describe the smooth surface reflectivity ($R_{\mathrm{ss},P}$) as a function of the dielectric constant of the soil (k) and the incidence angle (u) as follows:

$$R_{\mathrm{ss},[V]} = \left|\frac{k\cos u - \sqrt{k-\sin^2 u}}{k\cos u + \sqrt{k-\sin^2 u}}\right| \quad (4)$$

$$R_{\mathrm{ss},[H]} = \left|\frac{\cos u - \sqrt{k-\sin^2 u}}{\cos u + \sqrt{k-\sin^2 u}}\right|. \quad (5)$$

The dielectric constant of the soil is related to SM and can be modeled with dielectric mixing models (e.g., [39], [40], [41]). The rough surface reflectivity can be calculated from the smooth surface reflectivity using the Q parameter for cross polarization mixing and h for the roughness length [42] according to the following equations:

$$R_{\mathrm{rs},[V]} = \left(QR_{\mathrm{ss},[H]} + (1-Q)R_{\mathrm{ss},[V]}\right)\exp^{-\mathrm{hcos}(u)} \quad (6)$$

$$R_{\mathrm{rs},[H]} = \left(QR_{\mathrm{ss},[V]} + (1-Q)R_{\mathrm{ss},[H]}\right)\exp^{-\mathrm{hcos}(u)}. \quad (7)$$

According to Meesters et al. [43], the MPDI can be expressed as a function of vegetation and soil emissivity using the τ–ω model in combination with a set of assumptions: 1) the soil (T_s) and vegetation canopy temperatures (T_v) are assumed to be equal; 2) both vegetation parameters τ_v and ω are considered independent of polarization; and 3) the atmospheric contribution to the MPDI is assumed to be negligible. Under these assumptions, the MPDI can be modeled as follows:

$$\mathrm{MPDI}_{\tau-\omega} = \frac{e_{\mathrm{rs},[V]} - e_{\mathrm{rs},[H]}}{2a + e_{\mathrm{rs},[V]} + e_{\mathrm{rs},[H]}} \quad (8)$$

where

$$2a = \frac{2\left(1-\Gamma_v^2\right)}{2d\Gamma_v + \Gamma_v^2} \quad (9)$$

and

$$d = \frac{1}{2}\frac{\omega}{1-\omega}. \quad (10)$$

B. MPDI Analysis

At the start, a simulation was conducted using the $\mathrm{MPDI}_{\tau-\omega}$ model, as described in (8)–(10). This analysis was done to demonstrate its sensitivity for vegetation, SM, surface roughness, and incidence angle.

Then, multiangle passive microwave measurements at 10.7, 19.35, and 37.1 GHz from aircraft scans over land were analyzed. The MPDI was calculated for each brightness temperature observation based on (1) and its angular dependence was examined. A signal-to-noise ratio (SNR) for the MPDI was calculated for each flight day to assess the retrieval skill of each frequency, the role of incidence angle, and the overall stability of the instrument across flights. This SNR was calculated using the following equation:

$$\mathrm{SNR} = 10\log_{10}\left(\frac{\sigma^2_{40°-45°}}{\sigma^2_{0°-5°}}\right) \quad (11)$$

where SNR is expressed in decibels (dB). Noise was determined from the variance (σ^2) of the MPDI in the range of 0°–5°. Within this angle range (i.e., close to nadir), the microwave radiation emitted from a surface is not polarized [44], and the horizontally and vertically polarized brightness temperatures are assumed to be equal. Therefore, the variation of the MPDI within this range is taken as representative of the noise. At higher angles, the emitted microwave radiation from a surface is partly polarized. The degree of polarization depends on the soil dielectric constant and the incidence angle and can be estimated by means of the Fresnel relations as shown by (4) and (5). When the soil is characterized by a random rough surface, the degree of polarization depends on the roughness parameters as well and decreases as the roughness increases [as illustrated in (6) and (7)]. The polarization difference is largest and most sensitive to SM at the highest angles. Therefore, the range of 40°–45°, where the MPDI exhibited its highest amplitude, is used to calculate the variance. The variance of the MPDI over this range is considered the signal.

After the calculation of the SNR, the $\mathrm{MPDI}_{\tau-\omega}$ model was used to fit the measured MPDI for the individual scan lines perpendicular to the flight direction (i.e., 25 measurements from 0° to 45° over a 20-km strip). The model was optimized for angles between 25° and 45° by minimizing the root-mean-square error (RMSE) between the observed and simulated MPDI over a range of soil dielectric constant (k) and vegetation optical depth (τ_v) values. Both model performance and the retrieval accuracy of the geophysical parameters were evaluated.

In addition to the $\mathrm{MPDI}_{\tau-\omega}$ model, an empirical RM was applied to characterize the angular linearity of the MPDI with observations between 25° and 45°. The RMSE between the observations and a linear fit of the data was calculated, and the performance of this approach was evaluated by comparing its RMSE to that of the radiative transfer model (i.e., $\mathrm{MPDI}_{\tau-\omega}$). Statistical analyses were conducted on all scans to assess the presence of linearity across the different frequencies. The angular linearity was further investigated by extrapolating the derived linear regression to 55° using AMPR data and comparing it with independent AMSR2 MPDI satellite measurements

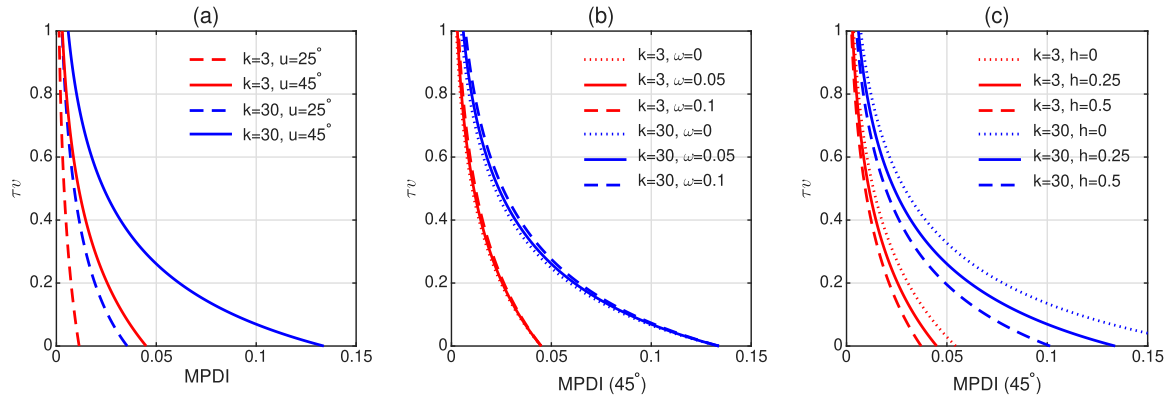

Fig. 4. Simulations of $\text{MPDI}_{\tau-\omega}$ for dry (k = 3, red) and wet (k = 30, blue) conditions over a range vegetation optical depth values (τ_v) with different (a) incidence angles, (b) single scattering albedo values (ω), and (c) surface roughness length (h).

at all three frequencies. A clear 1:1 relationship would be expected if the MPDI exhibited angular linearity.

For each scan, the linear angular slope of the MPDI was determined from AMPR observations between 25° and 45° and compared with SM and vegetation variations derived from SMAP and MODIS, respectively. The slope was expressed as ΔMPDI, representing the change in MPDI per degree of incidence.

The ΔMPDI derived from the AMPR data was compared with the ΔMPDI calculated from SMOS for the flight days during which the two datasets overlapped. The similarity between the AMPR- and SMOS-derived ΔMPDI values was examined. This analysis was conducted to obtain an initial assessment of the effects of scale, frequency, and instrument architecture. Details on the derivation and presentation of the SMOS ΔMPDI can be found in Appendix B.

Finally, a series of RMs was tested to assess whether ΔMPDI could serve as an additional indicator of SM. In these models, SMAP SM was used as a reference. The models employed the following equation:

$$\text{AMPR SM} = C_1 x_1 + C_2 x_2 + C_3 \tag{12}$$

where x_1 and x_2 denote the input parameters and C_1–C_3 represent the derived coefficients. AMPR SM is the derived SM in $\text{m}^3 \cdot \text{m}^{-3}$ from AMPR measurements. Four RMs were tested. RM1 used only ΔMPDI as x_1; RM2 used the NDVI as x_2 in addition to ΔMPDI as x_1; RM3 used the average horizontally polarized brightness temperature over the 25°–45° range as x_2; and RM4 uses the average vertically polarized brightness temperature as x_2.

In this study, scatter density plots were used to reveal potential structures that may be obscured by the large number of data points.

V. Results

A. MPDI Modeling

The $\text{MPDI}_{\tau-\omega}$ model was used to investigate the sensitivity of the MPDI. The model simulated MPDI values for a range of vegetation optical depth values for dry (k = 3) and wet (k = 30) conditions with different input parameters. Fig. 4 provides a graphical representation of the simulations. As an initial setup, a cross polarization mixing value (Q) of 0.1, a single scattering albedo (ω) of 0.05, and a surface roughness length (h) of 0.25 were used. These parameters were adopted from the ESA Climate Change Initiative (CCI) baseline algorithm for SM [45]. In Fig. 4(a), the influence of incidence angle is illustrated with a substantial reduction in sensitivity to SM and vegetation optical depth when the incidence angle is reduced from 45° to 25°. The influence of the single scattering albedo on this relationship is limited, as shown in Fig. 4(b), with a fixed incidence angle of 45°. However, surface roughness length (h) does have an influence on the relationship [as illustrated in Fig. 4(c)]. A smooth surface (h = 0) would provide the highest sensitivity to SM and vegetation optical depth, whereas a rough surface (h = 0.5) would reduce it.

The dual-polarized brightness temperatures, as measured by AMPR on October 22, were converted to MPDI values and plotted against the incidence angle. Fig. 5 presents this relationship for the three frequencies. The MPDI at 10.7 GHz shows the largest MPDI range at higher incidence angles, reaching up to 0.08. At 19.35 GHz, this range decreases to approximately 0.065, and at 37.1 GHz, the range further decreases to 0.06. These findings are consistent with [46], which explained the difference in the MPDI range by stronger vegetation attenuation at higher frequencies (i.e., a given vegetation cover would have higher τ_v values at higher frequencies). The density plot at 37 GHz at one scan side, as shown in Fig. 5(c), is different than the other side [see Fig. 5(f)], particularly between 10° and 40°. This difference occurs only at this frequency and might be related to the minor cross-track sinusoidal noise signal detected at this frequency, as described in [28]. In addition, the MPDI at 10.7 GHz appears more scattered than for other frequencies. For the other two days, the scatter density plots appear similar (not shown).

Table I provides the estimated SNR for the MPDI at each frequency. The SNR varies from day to day, reflecting differences in conditions and flight lines. However, the order of magnitude is similar with high-SNR values for both 10.7 and 19.35 GHz and lower values for 37.1 GHz. With SNR values between approximately 20–30 dB, the MPDI signals

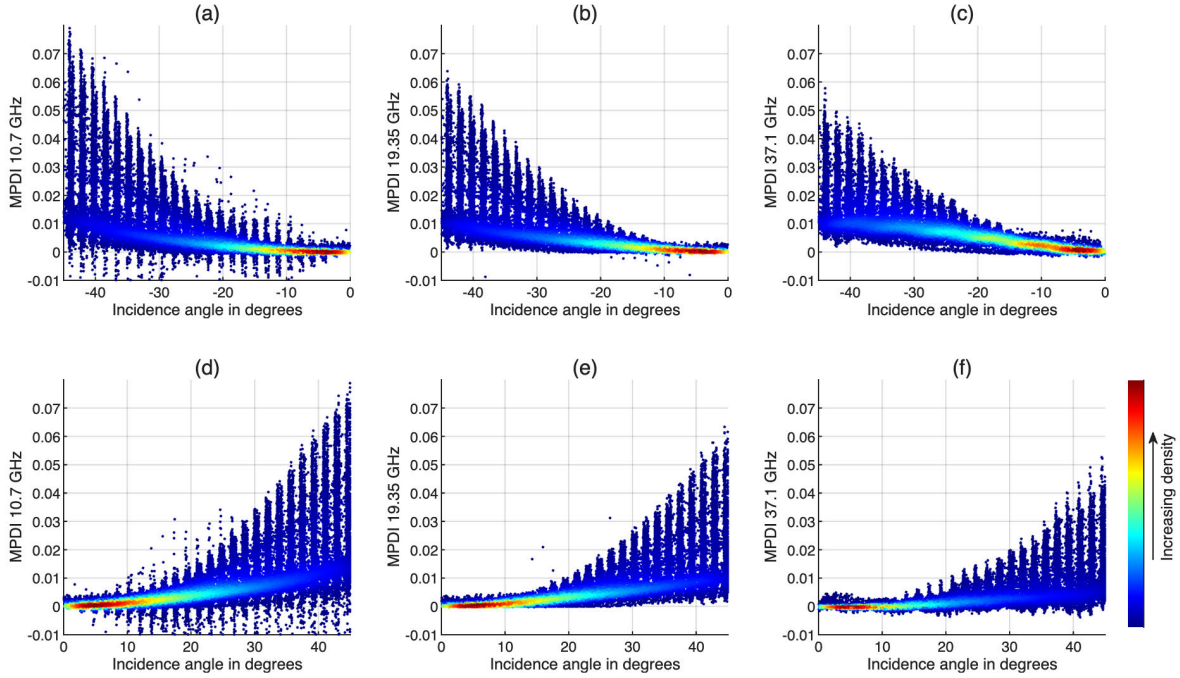

Fig. 5. Scatter density plots of the incidence angle compared to the AMPR MPDI measurements from October 22 for both sides of the scan for (a) and (d) 10.7 GHz, (b) and (e) 19.35 GHz, and (c) and (f) 37.1 GHz.

TABLE I
SNR OF THE MPDI FOR THE DIFFERENT FREQUENCIES CALCULATED FOR THE THREE DIFFERENT FLIGHTS

Frequency $[GHz]$	SNR 22/10 $[dB]$	SNR 25/10 $[dB]$	SNR 31/10 $[dB]$
10.7	30	27	28
19.35	31	29	26
37.1	24	19	20

from AMPR during these flights over land can be considered suitable for determining variations in SM and vegetation. The results also indicate that high incidence angles are required to derive vegetation and SM variations with the MPDI.

The measured MPDI at 10.7 GHz was simulated with the $\text{MPDI}_{\tau-\omega}$ model and the RMSE between the observed and $\text{MPDI}_{\tau-\omega}$ model at angles between 25° and 45° was calculated for a range of dielectric constant values, representing different SM conditions [i.e., from $k = 3$ (dry) to $k = 30$ (wet)], and vegetation densities represented by optical depth (τ_v) values ranging from 0 to 1. The surface roughness length, cross polarization mixing, and scattering effects were adopted from the ESA CCI baseline algorithm for SM [45], as previously described, with a cross polarization mixing of $Q = 0.1$, a roughness length value of $h = 0.25$, and a single scattering albedo of $\omega = 0.05$. Figs. 6 and 7 show model performance for two scans with different conditions. Fig. 6 illustrates an example of an agricultural area in OK (Lat = 36.2684°N and Lon = 97.799°W) with a sparse vegetation cover and dry and wet SM conditions. Fig. 7 shows the results for an agricultural area in OK (Lat = 35.8573°N and Lon = 98.3451°W) with denser vegetation. The dry conditions correspond to the first flight on October 22, and the wet conditions to October 31.

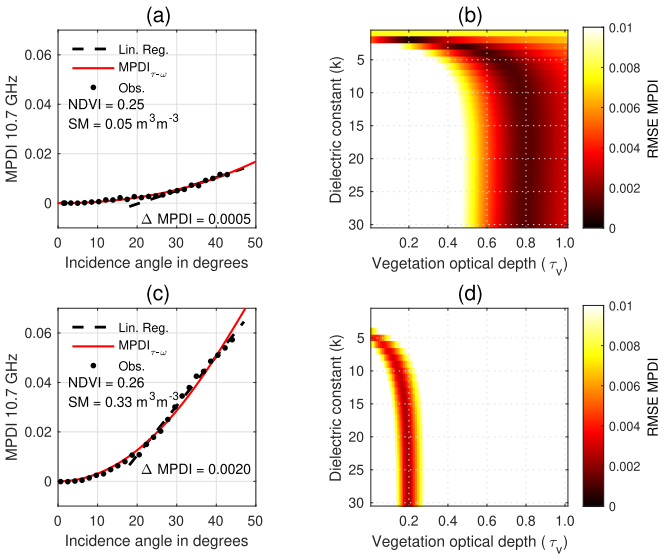

Fig. 6. A selected multiangle AMPR MPDI observation scan at 10.7 GHz over a 20-km swath with sparse vegetation conditions over an agricultural area in OK. Angular behavior during (a) and (b) dry conditions and (c) and (d) wet conditions. In (a) and (c), radiative transfer model simulation ($\text{MPDI}_{\tau-\omega}$) with the lowest RMSE is given in red, and the linear regression for the points between 25° and 45° is given as a dashed line. The calculated slope in MPDI per degree is added as ΔMPDI. (b) and (d) Variation in RMSE between $\text{MPDI}_{\tau-\omega}$ and observations for a range of dielectric constants and vegetation optical depth values. The SM values are derived from SMAP and the NDVI from MODIS.

These plots demonstrate that different combinations of dielectric constant and vegetation optical depth are possible with similar RMSE values. Dry conditions show a tight range in dielectric constants for low vegetation optical depth values

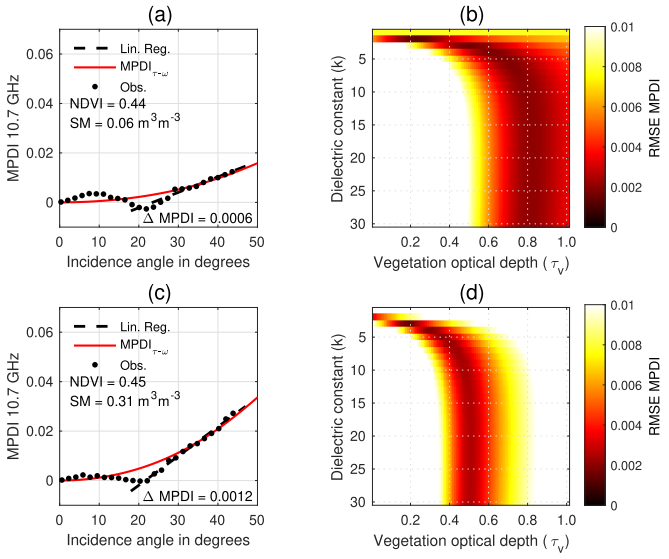

Fig. 7. Like Fig. 6 but for a scan over a 20-km strip with a denser vegetation cover over an agricultural area in OK.

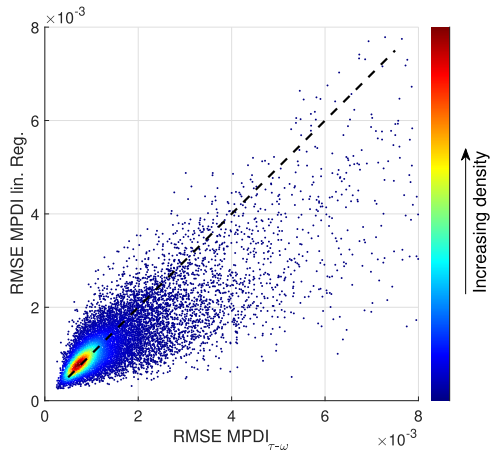

Fig. 8. Scatter density plot of the RMSE of the MPDI$_{\tau-\omega}$ model and the RMSE of the MPDI based on a linear regression. The 1:1 line is added as a dashed line for visualization purposes.

(i.e., $\tau_v < 0.5$), whereas wet conditions reveal a narrower range of vegetation optical depth at dielectric constant values above 10. The MPDI$_{\tau-\omega}$ model (indicated with a red line) represents the result with the lowest RMSE. The linear regression (black dashed line) and the derived ΔMPDI are also shown in these plots. ΔMPDI increases during wet conditions compared with dry conditions; this increase appears smaller under dense vegetation cover.

Both MPDI$_{\tau-\omega}$ and the linear RM were applied to all scans, and the calculated RMSE of each approach was compared. Fig. 8 provides the results of this comparison. The linear regression reveals a similar performance as the MPDI$_{\tau-\omega}$ model in terms of RMSE, with slightly more RMSE values of MPDI$_{\tau-\omega}$ lying below the 1:1 line.

B. Angular Linearity as a Tool

The observed linearity of MPDI over the incidence angle was further investigated, and the derived correlation coefficient, as part of the linear regression, was analyzed for each frequency. Table II provides a statistical summary of this analysis. For 10.7 GHz, a strong linearity was found with 87.5% of the 20 857 analyzed scans having an $R^2 > 0.7$. For an $R^2 > 0.9$, the percentage remained high at 71.2%. Low correlations were sparse and predominantly found in regions where the flight scan covered a heterogeneous landscape. At the other two frequencies, the percentages were lower, particularly at 37.1 GHz. This reduction is primarily attributable to the smaller MPDI range at these frequencies.

TABLE II

PERCENTAGE OF CALCULATED R^2 VALUES AS PART OF THE LINEAR REGRESSION BETWEEN THE MPDI AND THE INCIDENCE ANGLES BETWEEN 25° AND 45° BASED ON ALL FLIGHT SCANS

Frequency $[GHz]$	$R^2 > 0.7$ [%]	$R^2 > 0.8$ [%]	$R^2 > 0.9$ [%]
10.7	87.5	83.1	71.2
19.35	79.4	71.2	52.5
37.1	44.3	32.9	16.0

For each scan and each frequency, the calculated linear relationship was used to extrapolate the MPDI to 55°, which is the incidence angle of AMSR2. Fig. 9 presents the comparison between the extrapolated MPDI at 55° based on the AMPR data and the MPDI of AMSR2. Linear relationships close to the 1:1 line were observed across all frequencies, despite differences in footprint size, overpass time, observation frequency, and bandwidth. This analysis further confirms the strong angular linearity in the MPDI at these frequencies. This analysis was based on 6570 data pairs. The simulated 10.7-GHz AMPR MPDI at 55° provided a correlation coefficient (R^2) of 0.69 and an RMSE of 0.0107 relative to the AMSR2 MPDI. The statistics for the other frequencies were similar with lower RMSE values: R^2 = 0.78 and RMSE = 0.0075 for 19.35 GHz, and R^2 = 0.67 and RMSE = 0.0075 for 37.1 GHz.

The observed angular linearity can be captured by the ΔMPDI. The sensitivity of this new parameter to SM is illustrated in Fig. 10. The derived ΔMPDI values from 10.7 GHz are plotted for a transect between 103°W in TX and 97°W in OK, where the flight path was identical across three days, but SM conditions changed (particularly on October 31). A clear positive shift in ΔMPDI appeared as SM conditions changed, illustrating its sensitivity to SM variability. Between 100°W and 97°W, ΔMPDI exhibited greater fluctuations on October 31 than SMAP SM. This difference may be attributed to variations in spatial resolution. ΔMPDI originates from the 10.7-GHz observations with a 2.8-km footprint [23], whereas SMAP SM is derived from footprints with a resolution of approximately 40 km [47]. In addition, ΔMPDI is sensitive to vegetation (as shown in Figs. 6 and 7), and spatial patterns in vegetation density may influence the sensitivity of ΔMPDI to SM changes in this region.

The sensitivity of ΔMPDI to both vegetation and SM for these three flights is illustrated in Fig. 11. In this scatter plot, ΔMPDI was plotted against the MODIS NDVI for four different SM classes as derived from SMAP. The graph reveals a similar pattern to that shown in the MPDI simulations (i.e.,

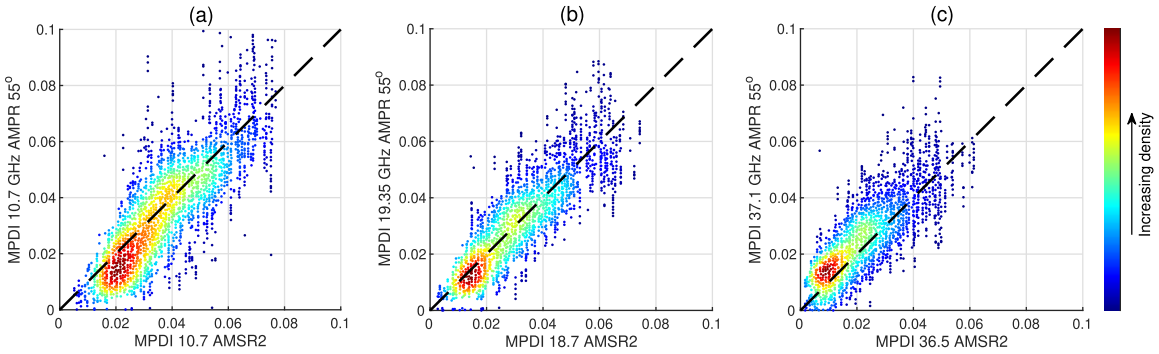

Fig. 9. Scatter density plots of AMSR2 MPDI versus simulated MPDI from AMPR at 55° based on linear extrapolation for (a) 10.7-GHz measurements, for both (b) 18.7 AMSR2 versus 19.35-GHz AMPR and (c) 36.5 AMSR2 versus 37.1-GHz AMPR.

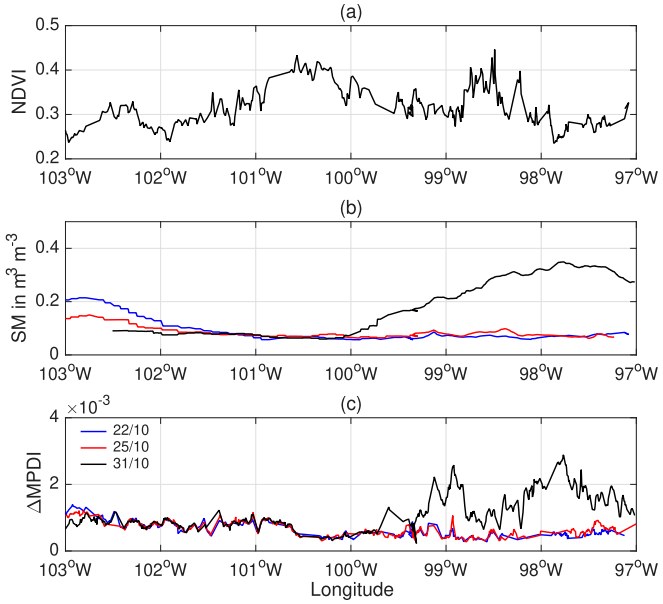

Fig. 10. Vegetation, SM, and ΔMPDI variations along the longitudinal bands from TX to OK for the three different flights. (a) 16-day NDVI from MODIS. (b) SMAP SM conditions for October 22, 25, and 31. (c) ΔMPDI for the same days.

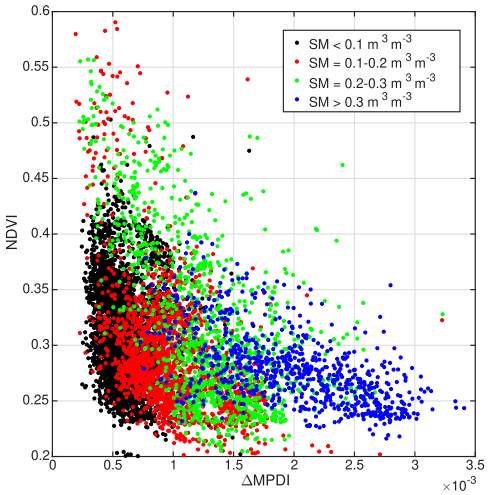

Fig. 11. Scatterplot of the ΔMPDI of AMPR and the MODIS NDVI for four different SM classes based on SMAP data.

Fig. 4). Due to the presence of low-NDVI values (NDVI <0.3) over the flight lines, representing relatively sparse vegetation covers, ΔMPDI appears to be primarily sensitive to SM. For NDVI values >0.3, the sensitivity to SM starts to decline.

On both October 22 and 25, there were regions within the flight lines where SMOS and AMPR overlapped. SMOS is the only low-frequency multiangle microwave satellite in orbit, and the ΔMPDI of SMOS at L-band (1.4 GHz) was calculated and compared with the ΔMPDI at 10.7 GHz of AMPR for these regions. On October 22, the overlapping region covered an area between 110°W and 100°W. On October 25, the region was slightly farther to the east, covering an area between 106°W and 96°W. Fig. 12 represents the ΔMPDI of both microwave instruments over these two regions on these two days. Both ascending and descending SMOS data were available. The aircraft carrying AMPR flew the same flight lines on the return flight from east to west for both of these regions, which provided an opportunity to evaluate the consistency of the derived ΔMPDI. The longitudinal plots of ΔMPDI as derived from the ascending and descending SMOS measurements follow a similar pattern to that of AMPR. With ΔMPDI values up to 5×10^{-3}, the magnitude of the SMOS ΔMPDI was almost twice as large as AMPR. The ΔMPDI of AMPR exhibited a higher spatial variability than SMOS ΔMPDI, although SMOS followed the general trend. The difference in variability is most likely caused by the difference in spatial resolution between the instruments. The SMOS data was stored in a 25 × 25-km grid, but the spatial resolution is similar to that of SMAP and on the order of 35–50 km. Fig. 12 also shows that the ΔMPDI of AMPR from the EW and WE flights was almost identical. The comparison yielded an $R^2 = 0.90$ and an RMSE of 1.9×10^{-4} for 779 ΔMPDI data pairs from the two flights on October 22 between 110°W and 100°W. For October 25, the values were similar with an $R^2 = 0.83$ and an RMSE of 1.4×10^{-4} for 808 data pairs for the flights between 106°W and 96°W. These statistics demonstrate the strong consistency of the ΔMPDI of AMPR at 10.7 GHz.

For 10.7 GHz, only the ΔMPDI values for which the linear relationship had an $R^2 > 0.9$ were selected. This selection criterion ensures focus on the most robust ΔMPDI values.

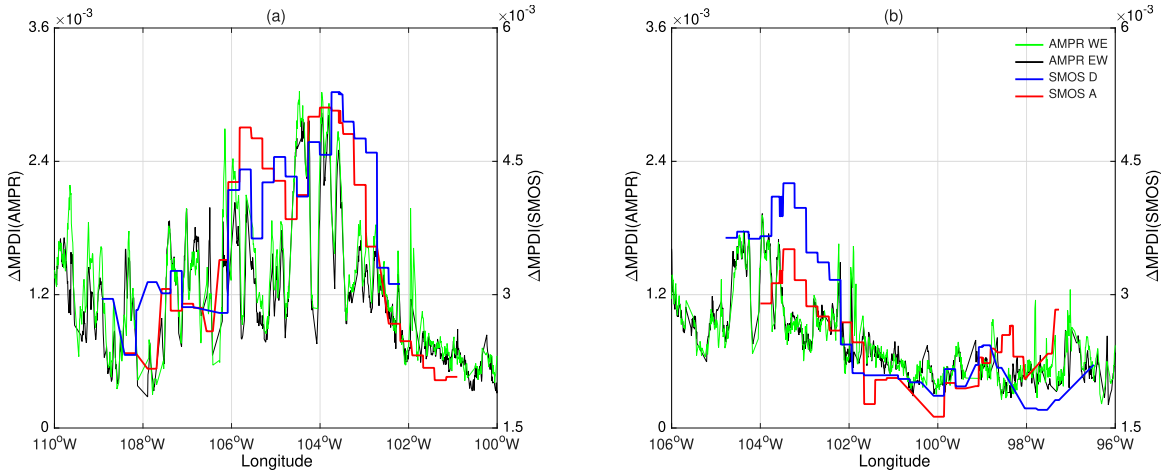

Fig. 12. ΔMPDI variations for AMPR and SMOS (A = ascending and D = descending) along longitudinal bands where the datasets overlapped for (a) October 22 and (b) October 25. Note that the west–east (WE) and east–west (EW) flights, during which AMPR data were collected, flew the same flight line on these days over these regions.

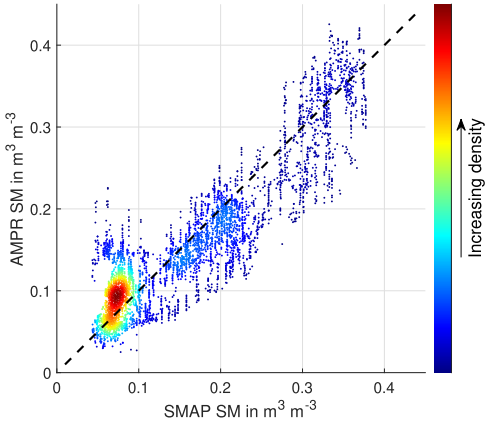

Fig. 13. Scatter density plot of SMAP SM and SM as derived from RM4 using AMPR data at 10.7 GHz.

TABLE III

STATISTICAL SUMMARY OF THE REGRESSION ANALYSIS FOR THE FOUR DIFFERENT RMS BASED ON 10.7-GHZ AMPR DATA

#	x_1	x_2	C_1	C_2	C_3	RMSE m^3m^{-3}	R^2
1	ΔMPDI	-	122.5	-	0.02	0.059	0.57
2	ΔMPDI	NDVI	140.4	0.416	-0.12	0.053	0.64
3	ΔMPDI	$T_{b,[H]}$	-4.44	-0.006	1.71	0.039	0.81
4	ΔMPDI	$T_{b,[V]}$	15.15	-0.007	2.04	0.038	0.81

The four different RMs, as described in Section IV, were applied to 7601 data pairs where both SMAP SM and the selected AMPR measurements were available. The summary of this analysis can be found in Table III. RM1, with only the ΔMPDI as input, already yielded an R^2 of 0.57 and an RMSE of 0.059 $m^3 \cdot m^{-3}$. There is an increase in the R^2 of 0.64 when vegetation information, in terms of NDVI, is added. Surprisingly, the biggest gain occurred when the original AMPR brightness temperatures are used, with a jump to R^2 values of 0.81 for both horizontally and vertically polarized brightness temperatures, respectively. This means that without using additional datasets such as MODIS NDVI, a high correlation can be achieved with only multiangle AMPR data. Fig. 13 provides a graphical visualization of the results from RM4, in which the SMAP SM is plotted against the derived AMPR SM. The data points in this graph are unevenly distributed along the dashed line, with a large cluster at low-SM values (around 0.1 $m^3 \cdot m^{-3}$), which illustrates a limitation of this analysis. The analysis was applied to the three flights, which exhibited reduced SM variability and primarily low vegetation densities (i.e., most MODIS NDVI values along the flight lines were below 0.4). As such, more tests are needed to determine the robustness of the approach. When RM4 was applied to 19.35-GHz data with similar selection criteria for ΔMPDI (i.e., only using ΔMPDI values with $R^2 > 0.9$), an R^2 of 0.74 was achieved with an RMSE of 0.048 $m^3 \cdot m^{-3}$ for 4959 data pairs. The performance was lower at this frequency than at 10.7 GHz, but the difference was relatively small.

VI. DISCUSSION

A. Signal-to-Noise Ratio

In this study, the calculation of SNR for the MPDI was introduced. By combining low- and high-angle measurements, it was possible to determine both the MPDI noise and the signal. This represents a clear added value of multiangle measurements, since this simple analysis allows insights into retrieval skill solely from observations. This information could potentially be used in data assimilation schemes where uncertainty values are a requirement [48], [49], [50]. Here, the overall SNR was calculated on a daily basis, but it could eventually also be applied to time series. In addition, this approach highlighted the capability of each frequency. At 19.35 GHz, the SNR was the highest on two days, despite the largest MPDI range at high angles occurring at 10.7 GHz. This high MPDI SNR could be linked to improved SM retrieval skill and likely explains why the correlation coefficient (R^2) between AMPR SM and SMAP SM based on RM4 remained high at this frequency (R^2 = 0.74 for 19.35 GHz versus R^2 = 0.81 for 10.7 GHz). This high SNR indicates that the instrument remains capable of retrieving reliable information,

despite the reduction in SM retrieval accuracy caused by vegetation attenuation.

B. Radiative Transfer

The MPDI has been used in several models to retrieve vegetation and SM dynamics [24], [25], [51]. However, these models have predominantly been optimized for measurements from single-angle observations [45], [52] or selected angle bins [53], [54] and used additional strategies to split the vegetation and SM contribution. For example, Owe et al. [24] used the MPDI in combination with a radiative transfer model for the horizontally polarized brightness temperature, incorporating additional temperature information to derive both SM and vegetation optical depth. Meng et al. [51] used normalized brightness temperatures and emissivities in combination with the MPDI to derive an SM index. Here, the behavior of the MPDI over multiple incidence angles was specifically investigated.

The optimized $\text{MPDI}_{\tau-\omega}$ model applied to the multiangle MPDI observations demonstrated a good performance, comparable to that of the linear RM, with RMSE values below 0.002 in most simulations, as shown in Fig. 8. Model simulations (as shown in Fig. 4) demonstrate the limited sensitivity to the single scattering albedo (ω), and a strong sensitivity to surface roughness length (h). The surface roughness length (h) has a similar influence on the model as the dielectric constant (k). When the model was optimized with a fixed surface roughness length and single scattering albedo, it did not produce a unique soil dielectric constant (k)–vegetation optical depth (τ_v) combination with the lowest RMSE but instead yielded a series of plausible solutions, each with a similarly low RMSE. If the surface roughness length (h) had been set as a dynamic parameter in the optimization routine, even more solutions would have been possible. Despite the low RMSE with the observations, the $\text{MPDI}_{\tau-\omega}$ model also relied on several assumptions, as described in Section IV-A. In particular, the assumption of equal soil and vegetation temperatures may not be valid and could affect model performance. In addition, the omission of high-order vegetation scattering and attenuation terms in the τ–ω approach could also cause a mismatch between the observations and the model. Therefore, we believe the $\text{MPDI}_{\tau-\omega}$ model has potential for improvement, and further research is required to clarify how it can be optimized and applied more effectively. The derivation of multiple plausible solutions for the vegetation optical depth (τ_v) and the soil dielectric constant (k) with the optimized $\text{MPDI}_{\tau-\omega}$ model can also be linked to a recently described phenomenon, which is called vegetation signal crosstalk [55], [56]. Vegetation and SM have an opposite influence on the microwave signal as shown in Fig. 4, and because of this contradicting influence, spurious vegetation signals can still remain in established SM products [55]. With the use of multiangle observations, we have a better understanding of how vegetation and moisture are represented in indices such as the MPDI. This understanding helps us further mitigate the vegetation crosstalk, which could lead to improved vegetation and SM products.

C. Angular Linearity

Angular linearity was identified in the AMPR MPDI observations and was characterized using a slope parameter, ΔMPDI. The calculation of this parameter for each scan was based on 11 observations between 25° and 45°, which produced a robust estimate. This robustness is illustrated in both Figs. 10 and 12, where the ΔMPDI provides a stable and consistent signal across three different days in both flight directions, except when SM conditions changed. The relationship of ΔMPDI with vegetation optical depth (τ_v) and the dielectric constant (k) might be comparable to that of a single-angle MPDI. Fig. 11, where ΔMPDI is plotted against NDVI for a series of SM classes, provided a similar relationship to that shown in the simulations in Fig. 4. The vegetation dynamics along the flight lines were relatively small, with primarily NDVI values below 0.4. These low values, which could be indicative of low vegetation densities, made ΔMPDI more sensitive to SM.

Therefore, simple RMs allowed realistic SM values to be derived. However, these results should be interpreted with caution. The analysis relied on just three flights over the United States with limited SM and vegetation dynamics. Additional analyses using other datasets could further support the hypothesis of linearity and the usefulness of parameterizing linearity. For example, the analysis on the multiangle MPDI relationship at L-band could be very useful, as multiangle data are available from multiple platforms, including ground-based observations [57], [58], aircraft campaigns [59], and satellite missions [8]. Such analyses could help to further verify the added value of multiangle observations. The analysis of a few days of SMOS data already revealed potential. In this small dataset, a clear angular linearity in MPDI was found, as shown in Fig. 12 and in Appendix B, Figs. 14 and 15, with high-value patterns up to 6×10^{-3} in both the descending and ascending passes. However, SMOS data are more complex compared with AMPR. The incidence angles are not equally distributed, with the majority of observations occurring around 40° as shown in Fig. 16 and the number of observations varies from 6 to 9 within a swath (see Figs. 14 and 15). Both the unequal distribution of angles and the variation in number of observations could affect the derivation of ΔMPDI, but the degree to which it affects the quality of the derived ΔMPDI estimate is still unknown. Therefore, when applying a methodology to derive ΔMPDI values over the entire SMOS archive, these effects need to be taken into account.

Despite the challenges, estimating the ΔMPDI and using this parameter in MPDI-based retrieval models such as [26] or [52] might be a valuable approach to investigate because, as shown in this study, the ΔMPDI produces a consistent signal derived from multiple observations. A more robust MPDI alternative, such as the ΔMPDI, could reduce the noise levels of SM retrievals, which are considered a major limitation in existing satellite-derived SM products [60]. SMOS data could be used to explore this.

In this study, the focus was on the MPDI because the influence of temperature is minimized with this index. One could also explore the angular relationship with land surface

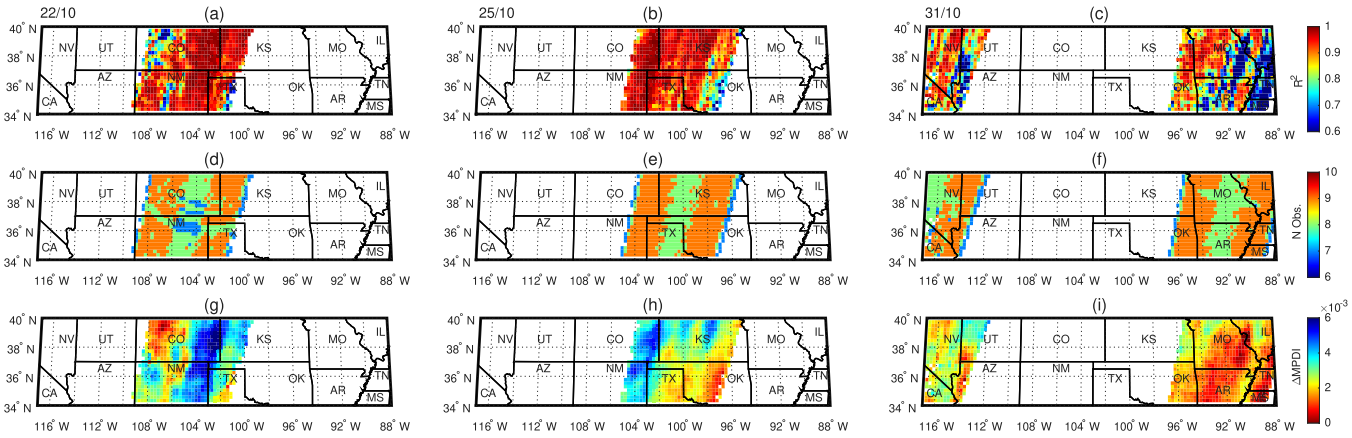

Fig. 14. Derivation of angular linearity in SMOS MPDI data based on the descending swath data of the three flight days. The correlation coefficient (R^2) is given in (a)–(c) for October 22, 25, and 31. (d)–(f) Provide the number of observations (N). (g)–(i) Derived ΔMPDI.

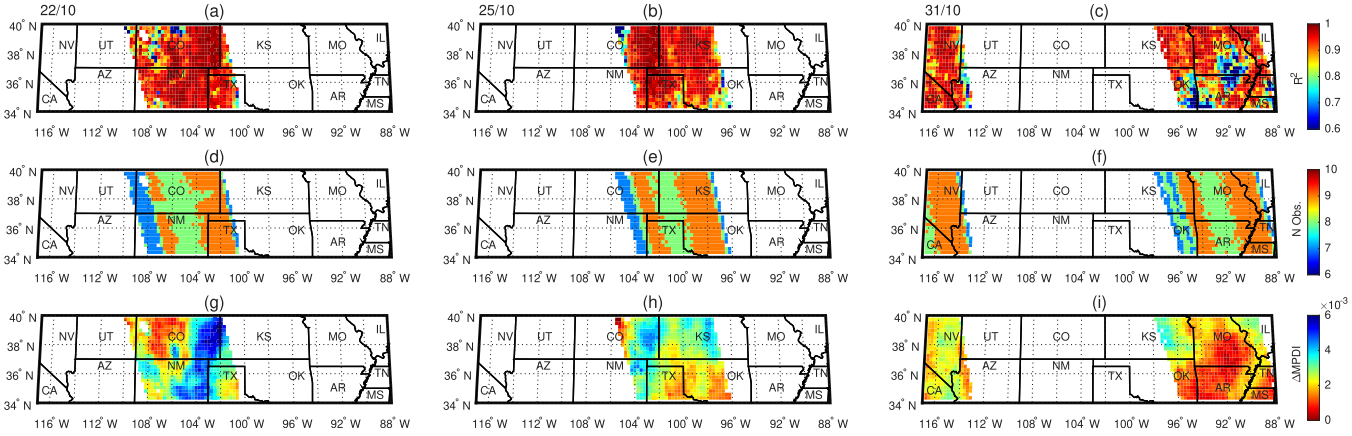

Fig. 15. Like Fig. 14 but now the results corresponding to the ascending SMOS data. The correlation coefficient (R^2) is given in (a)–(c) for October 22, 25, and 31. (d)–(f) Provide the number of observations (N). (g)–(i) Derived ΔMPDI.

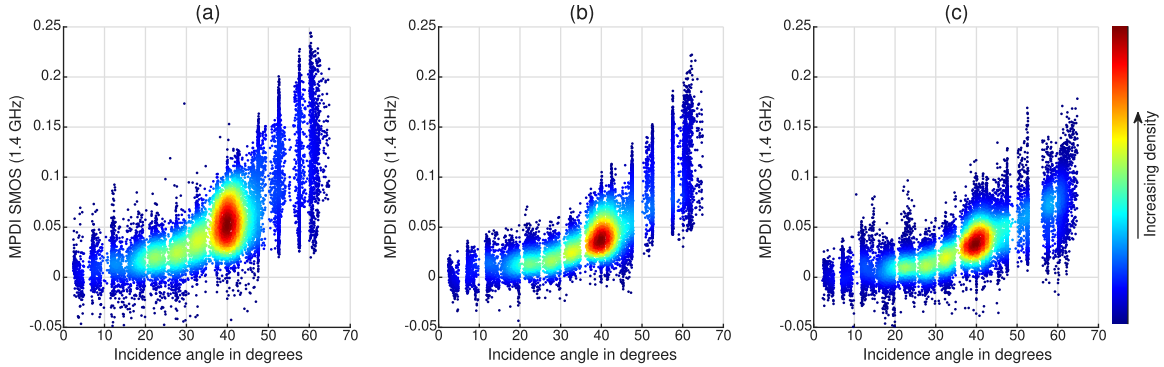

Fig. 16. Scatter density plots of the incidence angle compared to SMOS MPDI for the study region, for (a) October 22, (b) October 25, and (c) October 31. Both ascending and descending data are used in this plot.

emissivity for these flight observations. The advantage of using surface emissivity is that the effect of temperature is removed, and the relationship between incidence angle and surface emissivity has been well described in the literature (e.g., [44]). However, to extract reliable emissivity values from the observed brightness temperatures, accurate soil and vegetation temperatures are required. During the flights, these temperature values were not directly measured, and alternative datasets, such as MODIS land surface temperature, are needed to derive temperature estimates. These alternative datasets provide measurements at different times and have different spatial resolutions, which makes this option challenging to explore.

Furthermore, the results from this study indicate that it might also be possible to derive high-quality SM retrievals from higher frequencies than L-band using multiangle observations. Considering the observed linearity from 25° onward, only a few observations at fixed angles may be sufficient to

describe the full angular path of the MPDI. An instrument design in which a dual-polarized microwave radiometer measures at a selected set of angles could, therefore, offer an interesting and cost-effective alternative for SM monitoring.

VII. Conclusion

Dual-polarized passive microwave brightness measurements over land, acquired by AMPR during WH^{2}yMSIE, were analyzed to investigate whether multiangle observations can improve the retrieval of SM and vegetation information from passive microwave data. This research focused on the MPDI, a powerful index for detecting variations in SM and vegetation. MPDI measurements at incidence angles ranging from 0° to 45° for the 10.7, 19.35, and 37.1 GHz channels were collected over the United States during three flights in October 2024. The study demonstrated the added value of multiangle measurements, even though the datasets exhibited limited variation in SM and vegetation. The following conclusions can be drawn.

First, multiangle measurements allowed us to determine SNR values for the MPDI. These values provide insights into instrument performance and reveal the ability of each frequency to retrieve SM and vegetation dynamics.

Second, angular linearity of the MPDI was observed in the AMPR data. This linearity was reproduced by a τ–ω-based radiative transfer model and a linear RM, both exhibiting similar performance. Although the τ–ω-based radiative transfer model shows potential, it produced multiple plausible solutions and requires further investigation to improve convergence.

Third, the observed linearity was parameterized using a slope parameter, ΔMPDI. For the AMPR measurements, this parameter, which was based on multiple observations, appeared to be consistent in time and space, revealing similar patterns along flight lines acquired at different times. The ΔMPDI might have a similar relationship with SM and vegetation as a single-angle MPDI. For the study region, with measurements over low vegetation densities, the ΔMPDI of AMPR at 10.7 GHz was highly sensitive to SM.

Fourth, simple RMs demonstrated strong SM retrieval capabilities for these regions using only multiangle observations and their derivatives.

Overall, this study revealed insights into the behavior of multiangle passive microwave observations over land that were not visible in the single-angle satellite measurements. These insights can help us further enhance our knowledge of passive microwave measurements and could lead to more reliable microwave retrievals, such as SM.

Appendix A
Radiative Transfer Analysis for the Atmosphere

The atmospheric contributions along the flight path were simulated using the radiative transfer code of Boulder Environmental Sciences and Technology (BEST). The code has been validated against the community radiative transfer model (CRTM) [61] and has been shown to have a mean bias of less than 0.12 K and a standard deviation of errors less than 0.05 K in clear sky conditions at the relevant AMPR frequencies. Hourly ERA-5 data [62] were used as input for the model. A total of 3490 profiles were processed to estimate the atmospheric transmissivity (Γ_a) and the upwelling atmospheric contribution ($T_{b,\mathrm{au}}$) in Kelvin. For 10.7 GHz, Γ_a was 0.99 and $T_{b,\mathrm{au}}$ was 3 K with negligible variations. At 19.35 GHz, Γ_a was more variable and ranged from 0.95 to 0.98 with an average value of 0.97, while $T_{b,\mathrm{au}}$ ranged between 5 and 14 K with an average value of 8 K. At 37.1 GHz, the contribution was larger with Γ_a values ranging from 0.93 to 0.97 (average $\Gamma_a = 0.95$) and a $T_{b,\mathrm{au}}$ ranging from 9 to 20 K with an average value of approximately 13 K. All the flight paths were mostly free of any significant cloud liquid water, rain, or snow. The only exception occurred during the October 25 flight between 19:30 and 20:30 UTC as the aircraft turned around IL and MO. Therefore, according to the ERA-5 data, a total column cloud liquid water of approximately 0.3 kg·m^{-2} was present below the aircraft. Based on these findings, the atmospheric contributions to the MPDI have been considered negligible for this study.

Appendix B
Regression Analysis on SMOS

For the three flight days, the MPDI for SMOS was calculated using the horizontally and vertically brightness temperatures in (1). Each SMOS pixel provided multiple MPDI incidence angle pairs. Pairs with incidence angles greater than 25° were used to determine the angular linearity in the SMOS MPDI data. Fig. 14 shows the correlation coefficient (R^2), number of observations used (N) to determine the linear regression, and the derived ΔMPDI for the descending data. Fig. 15 shows the corresponding results for the ascending data.

In addition, both the ascending and descending MPDI incidence angle data pairs were collected for the given study region (i.e., between 34°N and 40°N, and −117°W and 88°W) and plotted for each day. Fig. 16 is similar as Fig. 5 but now with SMOS data for three different days. In these plots, both ascending and descending data were combined and used as one dataset.

References

[1] T. Schmugge, "Applications of passive microwave observations of surface soil moisture," *J. Hydrol.*, vols. 212–213, pp. 188–197, Dec. 1998.

[2] E. G. Njoku and D. Entekhabi, "Passive microwave remote sensing of soil moisture," *J. Hydrol.*, vol. 184, nos. 1–2, pp. 101–129, 1996.

[3] W. Wagner, G. Lemoine, and H. Rott, "A method for estimating soil moisture from ERS scatterometer and soil data," *Remote Sens. Environ.*, vol. 70, no. 2, pp. 191–207, Nov. 1999.

[4] W. Wagner et al., "The ASCAT soil moisture product: A review of its specifications, validation results, and emerging applications," *Meteorologische Zeitschrift*, vol. 22, no. 1, pp. 5–33, Feb. 2013.

[5] S. Hahn, C. Reimer, M. Vreugdenhil, T. Melzer, and W. Wagner, "Dynamic characterization of the incidence angle dependence of backscatter using metop ASCAT," *IEEE J. Sel. Topics Appl. Earth Observ. Remote Sens.*, vol. 10, no. 5, pp. 2348–2359, May 2017.

[6] A. Petchiappan, S. Steele-Dunne, M. Vreugdenhil, S. Hahn, W. Wagner, and R. S. Oliveira, "The influence of vegetation water dynamics on the ASCAT backscatter-incidence angle relationship in the Amazon," *Hydrol. Earth Syst. Sci. Discuss.*, vol. 26, pp. 2997–3019, 2022. [Online]. Available: https://doi.org/10.5194/hess-26-2997-2022

[7] J. Verspeek, A. Stoffelen, A. Verhoef, and M. Portabella, "Improved ASCAT wind retrieval using NWP ocean calibration," *IEEE Trans. Geosci. Remote Sens.*, vol. 50, no. 7, pp. 2488–2494, Jul. 2012.

[8] Y. H. Kerr et al., "The SMOS soil moisture retrieval algorithm," *IEEE Trans. Geosci. Remote Sens.*, vol. 50, no. 5, pp. 1384–1403, May 2012.

[9] Y. Bai et al., "A multi-temporal and multi-angular approach for systematically retrieving soil moisture and vegetation optical depth from SMOS data," *Remote Sens. Environ.*, vol. 280, Oct. 2022, Art. no. 113190.

[10] J.-P. Wigneron et al., "SMOS-IC data record of soil moisture and L-VOD: Historical development, applications and perspectives," *Remote Sens. Environ.*, vol. 254, Mar. 2021, Art. no. 112238.

[11] A. U. Schmitt and L. Kaleschke, "A consistent combination of brightness temperatures from SMOS and SMAP over polar oceans for sea ice applications," *Remote Sens.*, vol. 10, no. 4, p. 553, Apr. 2018.

[12] G. J. M. De Lannoy and R. H. Reichle, "Global assimilation of multiangle and multipolarization SMOS brightness temperature observations into the GEOS-5 catchment land surface model for soil moisture estimation," *J. Hydrometeorology*, vol. 17, no. 2, pp. 669–691, Feb. 2016.

[13] C. Donlon et al., "The Copernicus imaging microwave radiometer (CIMR): Mission overview and status," in *Proc. IEEE Int. Geosci. Remote Sens. Symp.*, Jul. 2024, pp. 6693–6696.

[14] J. Querol, A. Perez, and A. Camps, "A review of RFI mitigation techniques in microwave radiometry," *Remote Sens.*, vol. 11, no. 24, p. 3042, Dec. 2019.

[15] A. H. A. de Nijs, R. M. Parinussa, R. A. M. de Jeu, J. Schellekens, and T. R. H. Holmes, "A methodology to determine radio-frequency interference in AMSR2 observations," *IEEE Trans. Geosci. Remote Sens.*, vol. 53, no. 9, pp. 5148–5159, Sep. 2015.

[16] D. M. Le Vine and P. De Matthaeis, "Characteristics of RFI determined from kurtosis using the SMAP radiometer," *IEEE Trans. Geosci. Remote Sens.*, vol. 62, 2024, Art. no. 5300111.

[17] D. McKague, J. J. Puckett, and C. Ruf, "Characterization of K-band radio frequency interference from AMSR-E, WindSat and SSM/I," in *Proc. IEEE Int. Geosci. Remote Sens. Symp.*, Jul. 2010, pp. 2492–2494.

[18] G. Macelloni, S. Paloscia, P. Pampaloni, E. Santi, and M. Tedesco, "Microwave radiometric measurements of soil moisture in Italy," *Hydrol. Earth Syst. Sci.*, vol. 7, no. 6, pp. 937–948, Dec. 2003.

[19] X. Wu et al., "The P-band radiometer inferred soil moisture experiment 2019 workplan," Dept. Civil Environ. Eng., Monash Univ., Melbourne, VIC, Australia, Tech. Rep., 2019. [Online]. Available: https://www.prism.monash.edu/Data/PRISM-21/PRISM_2021%20Workplan.pdf

[20] J.-P. Wigneron, D. Guyon, J.-C. Calvet, G. Courrier, and N. Bruguier, "Monitoring coniferous forest characteristics using a multifrequency (5–90 GHz) microwave radiometer," *Remote Sens. Environ.*, vol. 60, no. 3, pp. 299–310, Jun. 1997.

[21] M. Guglielmetti, M. Schwank, C. Matzler, C. Oberdorster, J. Vanderborght, and H. Fluhler, "FOSMEX: Forest soil moisture experiments with microwave radiometry," *IEEE Trans. Geosci. Remote Sens.*, vol. 46, no. 3, pp. 727–735, Mar. 2008.

[22] A. Gambacorta et al., "The west-coast hyperspectral microwave sensor intensive experiment (WH^2yMSIE)," in *Proc. IEEE Int. Geosci. Remote Sens. Symp.*, Jul. 2024, pp. 1430–1432.

[23] R. W. Spencer et al., "High-resolution imaging of rain systems with the advanced microwave precipitation radiometer," *J. Atmos. Ocean. Technol.*, vol. 11, no. 4, pp. 849–857, Aug. 1994.

[24] M. Owe, R. de Jeu, and J. Walker, "A methodology for surface soil moisture and vegetation optical depth retrieval using the microwave polarization difference index," *IEEE Trans. Geosci. Remote Sens.*, vol. 39, no. 8, pp. 1643–1654, Aug. 2002.

[25] S. Paloscia, P. Pampaloni, and E. Santi, "Radiometric microwave indices for remote sensing of land surfaces," *Remote Sens.*, vol. 10, no. 12, p. 1859, Nov. 2018.

[26] J. Zeng, K.-S. Chen, C. Cui, and X. Bai, "A physically based soil moisture index from passive microwave brightness temperatures for soil moisture variation monitoring," *IEEE Trans. Geosci. Remote Sens.*, vol. 58, no. 4, pp. 2782–2795, Apr. 2020.

[27] C. G. Amiot, S. K. Biswas, T. J. Lang, and D. I. Duncan, "Dual-polarization deconvolution and geophysical retrievals from the advanced microwave precipitation radiometer during OLYMPEX/RADEX," *J. Atmos. Ocean. Technol.*, vol. 38, no. 3, pp. 607–628, Mar. 2021.

[28] T. Lang. (2025). *AMPR WH^2MSIE 2024 Science Dataset Level 2B*. [Online]. Available: https://www-air.larc.nasa.gov/cgi-bin/ArcView/whymsie#LANG.TIMOTHY/

[29] *NCEP FNL Operational Model Global Tropospheric Analyses, Continuing From July 1999 (updated Daily)*, National Centers for Environmental Prediction NCEP, 2024, doi: 10.5065/D6M043C6.

[30] J. Vivekanandan, J. Turk, and V. N. Bringi, "Comparisons of precipitation measurements by the advanced microwave precipitation radiometer and multiparameter radar," *IEEE Trans. Geosci. Remote Sens.*, vol. 31, no. 4, pp. 860–870, Jul. 1993.

[31] T. Maeda, Y. Taniguchi, and K. Imaoka, "GCOM-W1 AMSR2 level 1R product: Dataset of brightness temperature modified using the antenna pattern matching technique," *IEEE Trans. Geosci. Remote Sens.*, vol. 54, no. 2, pp. 770–782, Feb. 2016.

[32] *Application for Extracting and Exploring Analysis Ready Samples (AppEEARS)*. Accessed: Aug. 21, 2025. [Online]. Available: https://appeears.earthdatacloud.nasa.gov/

[33] M. J. Chaubell et al., "Improved SMAP dual-channel algorithm for the retrieval of soil moisture," *IEEE Trans. Geosci. Remote Sens.*, vol. 58, no. 6, pp. 3894–3905, Jun. 2020.

[34] J. Dong, W. T. Crow, and R. Bindlish, "The error structure of the SMAP single and dual channel soil moisture retrievals," *Geophys. Res. Lett.*, vol. 45, no. 2, pp. 758–765, Jan. 2018.

[35] A. Al Bitar et al., "The global SMOS level 3 daily soil moisture and brightness temperature maps," *Earth Syst. Sci. Data*, vol. 9, no. 1, pp. 293–315, Jun. 2017.

[36] *CATDS-PDC L3TB—Global Polarised Brightness Temperature Product From SMOS Satellite. (Updated Daily)*, CATDS, CNES, IFREMER, CESBIO, 2024, doi: 10.12770/6294e08c-baec-4282-a251-33fee22ec67f.

[37] M. J. Brodzik, B. Billingsley, T. Haran, B. Raup, and M. H. Savoie, "EASE-grid 2.0: Incremental but significant improvements for Earth-gridded data sets," *ISPRS Int. J. Geo-Inf.*, vol. 1, no. 1, pp. 32–45, Mar. 2012.

[38] T. Mo, B. J. Choudhury, T. J. Schmugge, J. R. Wang, and T. J. Jackson, "A model for microwave emission from vegetation-covered fields," *J. Geophys. Res., Oceans*, vol. 87, no. C13, pp. 11229–11237, Dec. 1982.

[39] M. Owe and A. A. Van de Griend, "Comparison of soil moisture penetration depths for several bare soils at two microwave frequencies and implications for remote sensing," *Water Resour. Res.*, vol. 34, no. 9, pp. 2319–2327, Sep. 1998.

[40] V. L. Mironov, M. C. Dobson, V. H. Kaupp, S. A. Komarov, and V. N. Kleshchenko, "Generalized refractive mixing dielectric model for moist soils," *IEEE Trans. Geosci. Remote Sens.*, vol. 42, no. 4, pp. 773–785, Apr. 2004.

[41] J. R. Wang and T. J. Chmugge, "An empirical model for the complex dielectric permittivity of soils as a function of water content," *IEEE Trans. Geosci. Remote Sens.*, vol. GRS-18, no. 4, pp. 288–295, Oct. 1978.

[42] J. R. Wang and B. J. Choudhury, "Remote sensing of soil moisture content, over bare field at 1.4 GHz frequency," *J. Geophys. Res., Oceans*, vol. 86, no. C6, pp. 5277–5282, Jun. 1981.

[43] A. G. C. A. Meesters, R. A. M. DeJeu, and M. Owe, "Analytical derivation of the vegetation optical depth from the microwave polarization difference index," *IEEE Geosci. Remote Sens. Lett.*, vol. 2, no. 2, pp. 121–123, Apr. 2005.

[44] F. T. Ulaby, R. K. Moore, and A. K. Fung, *Microwave Remote Sensing: Active and Passive. Volume 1-Microwave Remote Sensing Fundamentals and Radiometry*. Boston, MA, USA: Artech House, 1981.

[45] W. Dorigo et al., *ESA Climate Change Initiative Plus–Soil Moisture–Algorithm Theoretical Baseline Document (ATBD) Supporting Product Version 09.0, D2.4 Version 2.0*. Boston, MA, USA: Artech House, 2024.

[46] R. D. Jeu et al., "Analyzing satellite and airborne Ka-band passive microwave observations over land for temperature and vegetation monitoring," *Frontiers Remote Sens.*, vol. 6, p. 20, Apr. 2025.

[47] D. Entekhabi et al., "The soil moisture active passive (SMAP) mission," *Proc. IEEE*, vol. 98, no. 5, pp. 704–716, May 2010.

[48] R. H. Reichle, R. D. Koster, J. Dong, and A. A. Berg, "Global soil moisture from satellite observations, land surface models, and ground data: Implications for data assimilation," *J. Hydrometeorology*, vol. 5, no. 3, pp. 430–442, Jun. 2004.

[49] G. J. M. De Lannoy and R. H. Reichle, "Assimilation of SMOS brightness temperatures or soil moisture retrievals into a land surface model," *Hydrol. Earth Syst. Sci.*, vol. 20, no. 12, pp. 4895–4911, Dec. 2016.

[50] A. Gruber and R. H. Reichle, "Uncertainty estimation for SMAP level-1 brightness temperature assimilation at different timescales," *IEEE J. Sel. Topics Appl. Earth Observ. Remote Sens.*, vol. 15, pp. 9127–9145, 2022.

[51] X. Meng et al., "Validation and expansion of the soil moisture index for assessing soil moisture dynamics from AMSR2 brightness temperature," *Remote Sens. Environ.*, vol. 303, Mar. 2024, Art. no. 114018.

[52] M. Owe, R. de Jeu, and T. Holmes, "Multisensor historical climatology of satellite-derived global land surface moisture," *J. Geophys. Res., Earth Surf.*, vol. 113, no. F1, p. 17, Mar. 2008.
[53] R. A. M. de Jeu, T. R. H. Holmes, R. Panciera, and J. P. Walker, "Parameterization of the land parameter retrieval model for L-band observations using the NAFE'05 data set," *IEEE Geosci. Remote Sens. Lett.*, vol. 6, no. 4, pp. 630–634, Oct. 2009.
[54] R. V. D. Schalie, Y. H. Kerr, J. P. Wigneron, N. J. Rodríguez-Fernández, A. Al-Yaari, and R. A. M. D. Jeu, "Global SMOS soil moisture retrievals from the land parameter retrieval model," *Int. J. Appl. Earth Observ. Geoinf.*, vol. 45, pp. 125–134, Mar. 2016.
[55] W. T. Crow and A. F. Feldman, "Vegetation signal crosstalk present in official SMAP surface soil moisture retrievals," *Remote Sens. Environ.*, vol. 316, Jan. 2025, Art. no. 114466.
[56] S. Zwieback et al., "Estimating time-dependent vegetation biases in the SMAP soil moisture product," *Hydrol. Earth Syst. Sci.*, vol. 22, no. 8, pp. 4473–4489, Aug. 2018.
[57] P. de Rosnay et al., "SMOSREX: A long term field campaign experiment for soil moisture and land surface processes remote sensing," *Remote Sens. Environ.*, vol. 102, nos. 3–4, pp. 377–389, Jun. 2006.
[58] Z. Su et al., "Multiyear in-situ L-band microwave radiometry of land surface processes on the Tibetan Plateau," *Sci. Data*, vol. 7, no. 1, p. 317, Sep. 2020.
[59] L. F. White-Murillo et al., "Towards resolution enhancement of P-band brightness temperature data using passive-passive downscaling with L-band radiometer data," *Remote Sens. Environ.*, vol. 323, Jun. 2025, Art. no. 114737.
[60] H. E. Beck et al., "Evaluation of 18 satellite-and model-based soil moisture products using in situ measurements from 826 sensors," *Hydrol. Earth Syst. Sci.*, vol. 25, no. 1, pp. 17–40, 2021.
[61] B. T. Johnson, C. Dang, P. Stegmann, Q. Liu, I. Moradi, and T. Auligne, "The community radiative transfer model (CRTM): Community-focused collaborative model development accelerating research to operations," *Bull. Amer. Meteorological Soc.*, vol. 104, no. 10, pp. 1817–1830, Oct. 2023.
[62] H. Hersbach et al., "The ERA5 global reanalysis," *Quart. J. Roy. Meteorological Soc.*, vol. 146, no. 730, pp. 1999–2049, 2020.

Richard de Jeu (Member, IEEE) received the M.S. degree in environmental hydrology and the Ph.D. degree in Earth sciences from Vrije Universiteit Amsterdam, Amsterdam, The Netherlands, in 1996 and 2003, respectively.

From 2003 to 2015, he was an Associate Professor at Vrije Universiteit Amsterdam and developed multiple climate data records from satellite observations. In 2015, he founded the Earth observation company VanderSat, Haarlem, The Netherlands, which got acquired by Planet Labs, San Francisco, CA, USA, in 2021. He is currently the Director of the companies Transmissivity B.V., Alphen aan den Rijn, The Netherlands, and Radio Earth, Alphen aan den Rijn, The Netherlands. His research interests are in passive microwave remote sensing and the use of this technology for hydrological applications.

Susan S. Steele-Dunne received the S.M. and Ph.D. degrees in hydrology from Massachusetts Institute of Technology, Cambridge, MA, USA, in 2002 and 2006, respectively.

Since 2008, she has been with the Faculty of Civil Engineering and Geosciences, Delft University of Technology, Delft, The Netherlands.

She leads the M-WAVE Group, Delft, The Netherlands, who perform research from field to global scales, combining in situ and spaceborne sensors to improve our understanding of microwave interactions with vegetation. Her research interests include the use of data assimilation, modeling, and machine learning to exploit spaceborne microwave sensors for applications in ecosystem and agricultural monitoring.

Timothy Lang has been working with NASA since 2012, and before that, he was a Research Scientist at Colorado State University, Fort Collins, CO, USA. He has been serving as a Principal Investigator for the Advanced Microwave Precipitation Radiometer (AMPR) since 2014. In addition, he was an Aircraft Mission Scientist at the Westcoast and Heartland Hyperspectral Microwave Sensor Intensive Experiment (WH^2yMSIE) in 2024. He is the Lead Research Aerospace Technologist at the NASA Marshall Space Flight Center, Huntsville, AL, USA.

Corey G. Amiot was a Post-Doctoral Fellow of the NASA Postdoctoral Program at the NASA Marshall Space Flight Center, Huntsville, AL, USA, from 2023 to 2025, and a Graduate Research Assistant at The University of Alabama in Huntsville (UAH), Huntsville, from 2015 to 2023. His research focuses on active and passive microwave remote sensing of clouds and precipitation, and he has been working closely with the Advanced Microwave Precipitation Radiometer (AMPR) since 2018. He has supported AMPR operations during several field campaigns, including the 2024 Westcoast and Heartland Hyperspectral Microwave Sensor Intensive Experiment (WH^2yMSIE). He is a Research Scientist at the Earth System Science Center, UAH.

Marian Klein (Member, IEEE) received the M.S. and Ph.D. degrees in electrical engineering from the Technical University of Kosice (TU Kosice), Košice, Slovak Republic, in 1986 and 1996, respectively.

From 1987 to 1996, he was a Faculty Member with the Faculty of Electrical Engineering and Informatics, TU Kosice. From September 1996 to June 1997, he was a Fulbright Scholar at the Laboratory for Radio Science and Remote Sensing, Georgia Institute of Technology, Atlanta, GA, USA. From August 1998 to September 2007, he was a Research Associate with the Cooperative Institute for Research in Environmental Sciences (CIRES), University of Colorado Boulder, Boulder, CO, USA. In that capacity, he worked at the Microwave System Development Division, NOAA Environmental Research Laboratory, Boulder. Since the establishment of BEST in 2006, he has been the CEO of this innovative and growing company. The areas of his technical expertise include passive microwave remote sensing, radiative transfer theory, and the development of millimeter and submillimeter wave instrument systems for environmental studies.

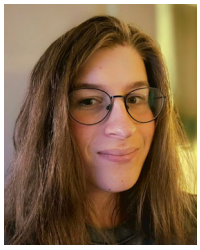

Madison Eble received the M.S. degree in aerospace engineering from the University of Colorado Boulder, Boulder, CO, USA, in 2016.

She has participated in research in the fields of aircraft deicing, spacecraft environmental systems, and zero-G fluid dynamics at the University of Colorado Boulder. She is a Mechanical and Aerospace Engineer at Boulder Environmental Sciences and Technology (BEST), Boulder, CO, USA. At BEST, she has worked on radiometer calibration, radiative transfer simulation development, and spacecraft material suitability.

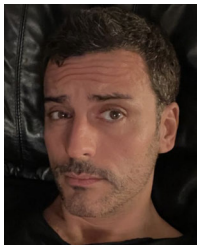

Diego G. Miralles is a Professor of hydrology and climate at Ghent University, Ghent, Belgium. He is an ecohydrologist and climate scientist recognized for advancing understanding in land–atmosphere interactions, with a particular focus on evaporation, soil moisture dynamics, biophysical processes, and their role in climate variability, extremes, and trends.